LARGE EDDY SIMULATION OF PARALLEL BLADE-VORTEX INTERACTION ON LOW REYNOLDS AIRFOIL

Antonella Abbà* and Andrea P.C. Bresciani
Politecnico di Milano - Dipartimento di Scienze e Tecnologie Aerospaziali , Milano - Italy
* antonella.abba@polimi.it

Abstract
In the present work the Large Eddy Simulation approach has been used to investigate the parallel interaction between a vortex and a SD7003 airfoil at angle of attack equal to 8° and Reynolds number 60000. The numerical code is based on the Local Discontinuous Galerkin finite element method associated with sophisticated anisotropic subgrid scale model. During the simulation, the polynomial degree has been adapted locally in space and dynamically in time on the base of the structure function indicator suitable for LES. The simulation shows the interaction with the vortex which stronghly affects the transitional separation on the airfoil and the force coefficients.

1 INTRODUCTION

The blade-vortex interaction (BVI) phenomenon is a relevant problem not only on helicopters in maneuvering conditions but also in the design of Micro Aerial Vehicle (MAV) and drones. The computational fluid dynamics represents an useful instrument to better comprehend the phenomenon. Parallel BVI has been studied with a RANS approach, coupled with a vorticity confinement method [1] to prevent an excessive diffusion of the advected vortex due to a poor resolution of the grid. Chimera method or overlapped grids approach have been also used in the same framework to predict BVI noise [2]. A hybrid RANS/LES method to study the parallel BVI has been applied by [3], however the first fully Large Eddy Simulation (LES) of a parallel blade–vortex interaction has been made by [4], where a simplified aeroelastic model has been presented. In order to deeply understand the mechanism of load generation related to the pressure field and three dimensional perturbations growth, to focus on the interaction between the vortex and the three dimensional structures in boundary layer and wake, accurate 3D unsteady numerical simulations of turbulent flows are necessary. For this reason it is very important the use of a numerical code based on high order schemes and a sophisticated subgrid scales model. In the present work a numerical code based on the Local Discontinuous Galerkin finite element method [5] associated with sophisticated anisotropic subgrid scale model [6], has been used to investigate the parallel interaction between a vortex and a SD7003 airfoil [7] at angle of attack equal to 8° and Reynolds number 60000, a regime of interest for MAV. During the simulation, the polynomial degree has been adapted locally in space and dynamically in time on the base of the structure function indicator [8] in order to save computational resources preserving the accuracy of the method. The parallel interaction between a vortex and a SD7003 airfoil at $\alpha = 8$, Reynolds number equal 60000 and Mach number 0.2 is investigated. The force coefficients during the BVI will be compared with the ones obtained in a simulation of the developed flow in the same conditions but without the vortex. As far as the author knowledge, there are not numerical simulation or experimental measurements in literature which can be used for a direct comparison. However some examples of similar works are presented in [3, 4]. Experimental studies on parallel BVI on the SD7003 airfoil have been made by [9]but they cannot be used for comparison, not only for the different Reynolds number, but, mostly, because two vortices are present in that experimental set-up.

In the following the numerical method are briefly resumed in Section 2, the setup of the numerical simulation and the results are discussed in the Section 3 and finally some conclusions are outlined in Section 4.

2 THE NUMERICAL MODEL

2.1 The Numerical Method

The filtered in space compressible Navier–Stokes equations, in non dimensional form, are considered to numerically simulate the BVI phenomenon in the present work. The filtered equations in compact form, suitable for simulation of turbulent compressible flow with the LES approach, read

$$\partial_t \mathbf{U} + \nabla \cdot \mathbf{F}(\mathbf{U}) = 0 \tag{1}$$

Presented at the 47th European Rotorcraft Forum, Glasgow, UK, 7-10 September, 2021

where $\mathbf{U} = [\overline{\rho}, \overline{\rho}\widetilde{\mathbf{u}}^T, \overline{\rho}\widetilde{e}]^T$ are the prognostic filtered variables density $\overline{\rho}$, momentum $\overline{\rho}\widetilde{\mathbf{u}}$ and total energy per unit volume $\overline{\rho}\widetilde{e} = \overline{\rho}(\widetilde{u}_i\widetilde{u}_i/2 + \widetilde{e}_i)$, sum of kinetic energy and internal energy $\overline{\rho}\widetilde{e}_i = \frac{1-k}{k}\widetilde{T}$. Here $k = c_p/R$, being R the ideal gas constant and $\widetilde{T}$ is the filtered temperature. The Favre filter operator $\widetilde{\cdot} = \overline{\rho\cdot}/\overline{\rho}$ is introduced bisides the space filter operator $\overline{\cdot}$, as usual in compressible LES to avoid additional subgrid terms in the mass conservation equation.

In the equation (1) the flux $\mathbf{F} = \mathbf{F}^{\mathrm{c}} - \mathbf{F}^{\mathrm{v}} - \mathbf{F}^{\mathrm{sgs}}$ contains the convective flux

$$\mathbf{F}^{\mathrm{c}} = \begin{bmatrix} \overline{\rho}\widetilde{\mathbf{u}} \\ \overline{\rho}\widetilde{\mathbf{u}} \otimes \widetilde{\mathbf{u}} + \frac{1}{\gamma Ma^2}\overline{p}\mathbb{I} \\ (\overline{\rho}\widetilde{e} + \overline{p})\widetilde{\mathbf{u}} \end{bmatrix}, \tag{2}$$

the viscous flux

$$\mathbf{F}^{\mathrm{v}} = \begin{bmatrix} 0 \\ \frac{}{Re}\mu\widetilde{\sigma} \\ \frac{\gamma Ma^2}{Re}\widetilde{\mathbf{u}}^T\widetilde{\sigma} - \frac{1}{kRePr}\widetilde{\mathbf{q}} \end{bmatrix} \tag{3}$$

and the turbulent modelled flux $\mathbf{F}^{\mathrm{sgs}}$. Here the Mach number Ma, the Reynolds number Re, the Prandtl number Pr and the specific heat ratio $\gamma = c_p/c_v$ appear. The constitutive relations

$$\sigma_{ij} = 2\mu(\widetilde{\mathcal{S}}_{ij} - \frac{1}{3}\widetilde{\mathcal{S}}_{kk}\delta_{ij}), \qquad q_i = \mu\partial_i\widetilde{T} \tag{4}$$

express the viscous stresses σ and the heat flux $\mathbf{q}$ in function of the strain rate tensor $\widetilde{\mathcal{S}}_{ij} = (\partial_i\widetilde{u}_j + \partial_j\widetilde{u}_i)/2$ and the Favre filtered temperature gradient respectively. The dynamic viscosity depends on the temperature according to the Sutherland's law $\mu = \widetilde{T}^{0.7}$. The system is closed by the equation of state for ideal gas $\overline{p} = \overline{\rho}\widetilde{T}$. The term $\mathbf{F}^{\mathrm{sgs}}$ represents the subgrid scale (sgs) fluxes for which a dynamic anisotropic model is provided.

The equation (1) is discretized in space by a finite element approach based on the Local Discontinuous Galerkin (LDG) [10] method. In the LDG method the previous equation is reduced to a first order system

$$\begin{aligned} \partial_t\mathbf{U} + \nabla\cdot\mathbf{F}(\mathbf{U},\boldsymbol{G}) &= 0 \\ \boldsymbol{G} - \nabla\varphi &= 0, \end{aligned} \tag{5}$$

by introducing the auxiliary variable $\boldsymbol{G}$ and where $\varphi = [\widetilde{\mathbf{u}}^T, \widetilde{T}]^T$. A tessellation $\mathcal{T}_h$ composed of non overlapping tetrahedral elements is defined in the numerical domain Ω over which a discontinuous finite element space $\mathcal{V}_h$

$$\mathcal{V}_h = \{v_h \in L^2(\Omega) : v_h|_K \in \mathbb{P}^{p_K}(K), \forall K \in \mathcal{T}_h\}, \tag{6}$$

is defined. Here $\mathbb{P}^{p_K}(K)$ denotes the space of polynomial functions of total degree p_K over the element K. The weak form of the equation (5) is discretized on the discontinuous finite element space using test functions belonging to the same space as the numerical solution. A modal DG approach is here applied by using a hierarchical orthonormal polynomial basis, obtained from the Legendre polynomials, for each element K in the finite dimensional space $\mathcal{V}_h$, for both the discontinuous finite element subspace and the prognostic unknowns, while symmetric quadrature rules [11] are applied to compute the projection in the physical space. Since the used formulae must be exact at least up to twice the polynomial degree q_K in each element K, the integrals on internal boundaries between two elements are computed using the maximum degree between the two elements when polynomial adaptivity is applied.

Since the grid filter $\overline{\cdot}$ is equivalent to the projection over the solution subspace [12, 13, 14], the filtered quantities can be identified with their numerical solution counterparts.

The Rusanov flux [15] is employed to compute the advectiv flux $\mathbf{F}^{\mathrm{c}}$ while centred fluxes are used for the diffusive fluxes $\mathbf{F}^{\mathrm{v}}$, $\mathbf{F}^{\mathrm{sgs}}$ and for the gradient variables $\{\varphi\}$ [16].

Moreover the explicit five stages fourth order Strong Stability Preserving Runge-Kutta method [17] is applied to advance in time the discretized filtered equations. This numerical model is implemented in a numerical code based on library `FEMilaro` [18], a generic finite element tool written using latest Fortran and MPI standards. A more detailed description of the numerical code can be found in [19].

2.2 The Anisotropic Sgs Model

The subgrid flux $\mathbf{F}^{\mathrm{sgs}}$

$$\mathbf{F}^{\mathrm{sgs}} = \begin{bmatrix} 0 \\ \tau^{sgs} \\ \frac{1}{k}\mathbf{Q}^{sgs} + \frac{\gamma Ma^2}{2}(J - \tau^{sgs}_{kk}\widetilde{\mathbf{u}}) \end{bmatrix}, \tag{7}$$

introduced in equation (7), is composed by the sgs stresses $\tau^{sgs}_{ij} = \overline{\rho u_i u_j} - \overline{\rho}\widetilde{u}_i\widetilde{u}_j$, the subgrid heat flux $\mathbf{Q}^{sgs} = \overline{\rho T\mathbf{u}} - \overline{\rho}\widetilde{T}\widetilde{\mathbf{u}}$ and the sgs turbulent diffusion flux $\mathbf{J}^{sgs} = \overline{\rho\mathbf{u}u_k u_k} - \overline{\rho}\widetilde{\mathbf{u}}\widetilde{u}_k\widetilde{u}_k$. All these terms are modelled using the anisotropic model presented in [20] and extended to compressible flows in [19, 6].

In the cited model the sgs tensor τ^{sgs} is assumed to be proportional to the strain rate tensor of the Favre filtered velocity field, through a fourth order symmetric tensor $\mathcal{B}$

$$\tau_{ij} = -\overline{\rho}\overline{\Delta}^2|\widetilde{\mathcal{S}}|\mathcal{B}_{ijrs}\widetilde{\mathcal{S}}_{rs}. \tag{8}$$

The filter size $\overline{\Delta}$ is determined elementwise as

$$\overline{\Delta}(K) = \sqrt[3]{\frac{Vol(K)}{n_\phi(K)+1}}. \tag{9}$$

where $n_\phi(K) = ((p_K+1)(p_K+2)(p_K+3)/6 - 1)$ is the number of basis functions required to span the polynomial space $\mathbb{P}^{p_K}(K)$ of degree p_K. The fourth order tensor $\mathcal{B}$ can be contracted in a second order symmetric tensors $\mathcal{C}$ by means of any rotation tensor. In particular, using the basis of the orthogonal Cartesian reference frame, we get

$$\tau^{sgs}_{ij} = -\overline{\rho}\overline{\Delta}^2\mathcal{C}_{ij}|\widetilde{\mathcal{S}}|\widetilde{\mathcal{S}}_{ij}. \tag{10}$$

The Germano's dynamic procedure [21] is then applied to determine the six independent element of the tensor $\mathcal{C}$. The

subgrid heat flux

$$Q_i^{sgs} = -\overline{\rho}\overline{\Delta}^2 C_i^Q |\widetilde{\mathcal{S}}| \partial_i \widetilde{T}, \tag{11}$$

and the subgrid diffusion flux

$$J_i^{sgs} = -\overline{\rho}\overline{\Delta}^2 |\widetilde{\mathcal{S}}| C_i^J \partial_i \left(\frac{1}{2} \widetilde{u}_k \widetilde{u}_k \right). \tag{12}$$

are modelled in a similar way and are computed at each time step with the dynamic procedure.

2.3 The Polynomial Adaptivity

The polynomial degree in each element can varies in space and time adatping himself to the local resolution requirement. The criterion to select the maximum polynomial degree in each element is based on an indicator sensitive to the local conditions of the turbulent flow and suitable for LES, presented in [8, 5]. This indicator is based on the structure function defined as

$$D_{ij} = < [u_i(\mathbf{x}+\mathbf{r},t) - u_i(\mathbf{x},t)] [u_j(\mathbf{x}+\mathbf{r},t) - u_j(\mathbf{x},t)] >,$$

to which the contribution due to homogeneous isotropic turbulence

$$D_{ij}^{iso}(\mathbf{r},t) = D_{NN}(r,t)\delta_{ij} + (D_{LL}(r,t) - D_{NN}(r,t)) \frac{r_i r_j}{r^2}$$

is removed. Here $< \cdot >$ represents the expected value operator and D_{LL}, D_{NN} are the longitudinal and transverse structure functions, respectively. The structure function is evaluated for each couple of element vertices and then averaged over the element. The structure function is directly related to the subgrid stresses and has been widely used to study turbulence statistics [22, 23, 24]. The structure function estimates how much the solution is fluctuating inside the element and where more resolution is required or where the reduction of the resolution in that element is possible.

The polynomial adaptativity indicator is then defined as:

$$Ind_{SF}(K) = \sqrt{\sum_{ij} [D_{ij}(K) - D_{ij}(K)^{iso}]^2}. \tag{13}$$

Although the structure function indicator (13) is more complex then other indicator based on the numerical error [25, 26], it could give more physical insight on the flow conditions.

In the simulations here presented, the maximum polynomial degrees in each element ranges between 2 and 4. If the indicator value is lower than a threshold ε_1 the maximum polynomial degree 2 is imposed, while the degree is limited to 4 if values higher than the threshold ε_2 are reached, and degree 3 is imposed for intermediate values. In the dynamic adaptive procedure the polynomials degrees can increase or decrease by one degree only. The computational load among the processors in a parallel run is balanced at the beginning of the simulation and at each restart on the basis of the adaptivity indicator obtained by the previous simulation, in order to avoid unbalanced load between computational processors.

3 NUMERICAL SIMULATION OF BVI

The described p-adaptive numerical code has been applied to the simulation of the parallel interaction between a vortex and a SD7003 infinite wing with angle of attack $\alpha = 8^\circ$, at a free-stream Mach number $Ma = 0.2$ and a Reynolds number $Re = 60000$ based on the chord. The airfoil is extruded 0.2 in the spanwise direction as in [27, 28]. The leading edge (LE) is located in the origin of the cartesian orthogonal reference frame. The non-slip, isothermal Dirichlet boundary condition with $T_w = 1$ is imposed on the airfoil. The inflow, the upper and lower boundaries are 5 unit from the LE while the position of the outflow surface is 10 units downstream the airfoil. The far field condition $U_\infty = (1,0,0)$ and $T = 1$ is imposed at the inflow, sponge layers have been applied on the outflow, on the upper and on the lower boundary to avoid reflections [29, 30] while cyclic boundary conditions are applied the in spanwise direction.

Then a vortex is introduced in the field developed around the airfoil to simulate the BVI phenomenon.

A vortex, with axis parallel to the wing and rotating in counterclockwise direction, has been introduced upstream the airfoil, overlapped to the developed velocity field obtained by a previous simulation .

The vortex is similar to those one defined in [31, 32] inducing the velocity and pressure

$$u = -\Gamma \frac{y}{R_v^2} \exp\left(\frac{-r^2}{2R_v^2}\right), \quad v = \Gamma \frac{x}{R_v^2} \exp\left(\frac{-r^2}{2R_v^2}\right), \quad w = 0,$$

$$p = p_0 \exp\left[\frac{-\Gamma^2}{2TR_v^2} \exp\left(\frac{-r^2}{R_v^2}\right)\right]$$

where Γ is the vortex circulation, r is the distance from the vortex centre and p_0 is the pressure in the statistically steady-state initial condition. The chosen values for the vortex radius $R_v = 0.05$ and $\Gamma = 0.0412$ are similar to values measured by [33].The vortex has been introduced in the position $(x_v, y_v) = (-1, -0.0166)$. The vortex starting from this position, slightly below the trailing edge (TE), hits the LE because of the induced velocity. It has been verified that one chord upstream is sufficient to avoid any initial influences of the vortex on the airfoil.

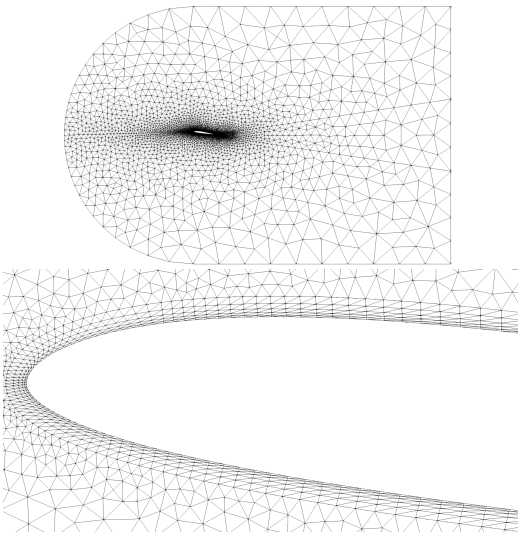

Figure 1: The two dimensional sketch of the computational mesh: the global view (top) and the detail of the structured layer around the airfoil (bottom)

A two dimensional sketch of the adopted grid is represented in Figure 1. A refinement line upstream the airfoil, to prevent the over dissipation of the vortex, is visible. A structured grid layer 0.01 thick has been designed around the airfoil. This structured layer is divided in $N_n = 5$ and $N_z = 8$ layers in normal to the wall and spanwise directions respectively. Each hexahedra obtained by this way is divided in 6 tetrahedral. The resulting grid with 110577 elements, corresponds to a resolution for polynomial degree 4 equal to $\Delta z = 1.38 \times 10^{-2}$ and $\Delta_n = 4.76 \times 10^{-4}$ in spanwise and normal to the wall direction respectively. The dynamic polynomial adaptivity have been applied considering the thresholds values $\varepsilon_1 = 10^{-4}$ and $\varepsilon_2 = 10^{-2}$. The SF indicator has been computed at time interval $\Delta t_{ind} = 4\Delta t$ where $\Delta t = 1.1 \times 10^{-5}$ is the computational time step, and then it was averaged over $\Delta t_{adapt} = 30\Delta t_{ind}$ before to update the polynomial degree distribution. These procedure ensure to accurately follow the vortex advected with a velocity comparable to the undisturbed one and to correctly represent the unsteady flow above the airfoil since the adaption interval is also much lower than the vortex shedding period on the transitional bubble.

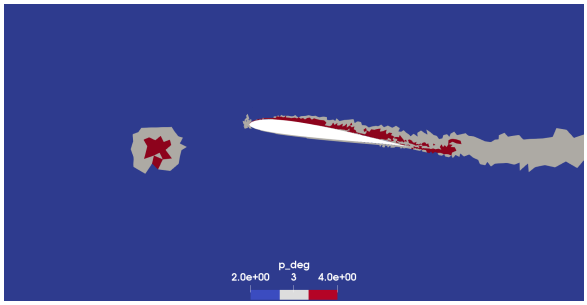

Figure 2: Polynomial degree distribution around the airfoil. The vortex approaching the airfoil is evident.

Figure 2 shows the resulting polynomial degree distribution when the vortex is approaching the airfoil.

3.1 Results

To evaluate the effect of the BVI the results of present simulations are compared to the ones obtained for the developed flow around the SD7003 wing in similar conditions but without the impinging vortex [34], considered as reference simulation. The developed flow around the SD7003 airfoil in these conditions is characterized by a short laminar separation bubble close to the LE with a turbulent reattachment. The position ξ_s of the boundary layer separation, ξ_t of the transition and of the reattachment ξ_r, evaluated along the chord, together with force coefficients, resulting by the reference simulation without BVI are reported in Table 1 demonstrating good agreement with literature results. A remarkable difference between the reference simulation and the literature is found for the reattachment position: this could be related to the fact that the ILES presents an essentially dissipative behavior while the dynamic anisotropic model used in the reference simulation is suitable to reproduce the backscatter phenomenon, fundamental for a correct simulation of transitional separated flow.

The transitional bubble is clearly depicted in Figure 3(a) representing the streamlines and the x component of the velocity averaged in spanwise direction, at the instant $t = 0.8$, before the influence of the approaching vortex is manifesting. The instability of the separated shear layer and its transition to turbulence is visible in Figure 4(a) representing the spanwise component of the vorticity vector at the same instant $t = 0.8$. The instantaneous field of the streamline velocity component represented in Figure 5(a) is also interesting. Here we see the stagnation point located just below the nose, the separation of the laminar boundary layer on the suction side, an intense negative velocity in the separated region, and then the reattachment of the turbulent boundary layer.

The type of BVI here considered is usually called viscous interaction because of the collision of the viscous core of the vortex on the LE. After the impact, the primary vortex splits into two secondary vortices which are advected downstream and, eventually, break down into smaller scales structures [36]. This behaviour is well represented in Figure 4(b) representing the spanwise vorticity at $t = 1.1$: the vortex hitted on the nose has splitted and on the suction side, where the effect is more intense, it is broken down in small vortices. Looking at the streamlines in Figure 3(b) and at the streamwise velocity in Figure 5(b), at the same instant $t = 1.1$, it is possible to see a separation region stronger, shorter and anticipated respect to that one of the undisturbed developed flow. The transitional bubble characteristic of the SD7003 flow is not more present and it is substituted by a disturbed attached boundary layer. In Figure 4(c) it is evident that the vortex shedding of the statistically steady-state condition is not yet reestablished.

Table 1: Results of the simulation of the developed flow on the SD7003 airfoil [34] taken as reference simulation. C_l, C_d, C_m are the lift, the drag and the moment coefficients respectively. ξ indicates the coordinate parallel to the chord; ξ_s, ξ_t, ξ_r are the positions of the separation, of the transition and of the reattachment above the transitional bubble. Some results from literature are also reported.

	Mach	C_l	C_d	C_m	ξ_s	ξ_t	ξ_r
Reference $\mathbb{P}$-adapt. LES [34]	0.2	0.9693	0.0346	-0.0186	0.038	0.1	0.175
Experimental [7]	< 0.01	0.936	0.0299	-	-	-	-
$\mathbb{P}$-adapt. ILES [35]	0.1	0.9270	0.0470	-	0.0301	-	0.3123
$\mathcal{O}(4)$ ILES [28]	0.2	0.968	0.034	-	0.037	0.105	0.20

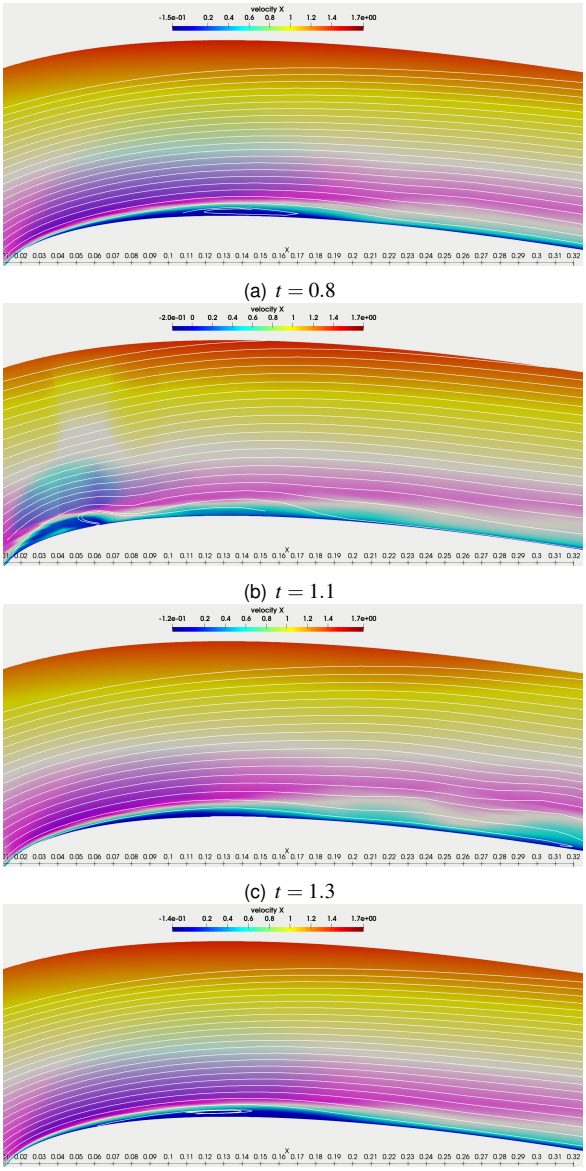

(a) $t = 0.8$

(b) $t = 1.1$

(c) $t = 1.3$

(d) $t = 1.6$

Figure 3: Streamlines for the spanwise averaged velocity field above the separation bubble; from top to the bottom: before the hit of the vortex, at the instants corresponding to the maximum and the minimum lift and when the vortex is passed downstream.

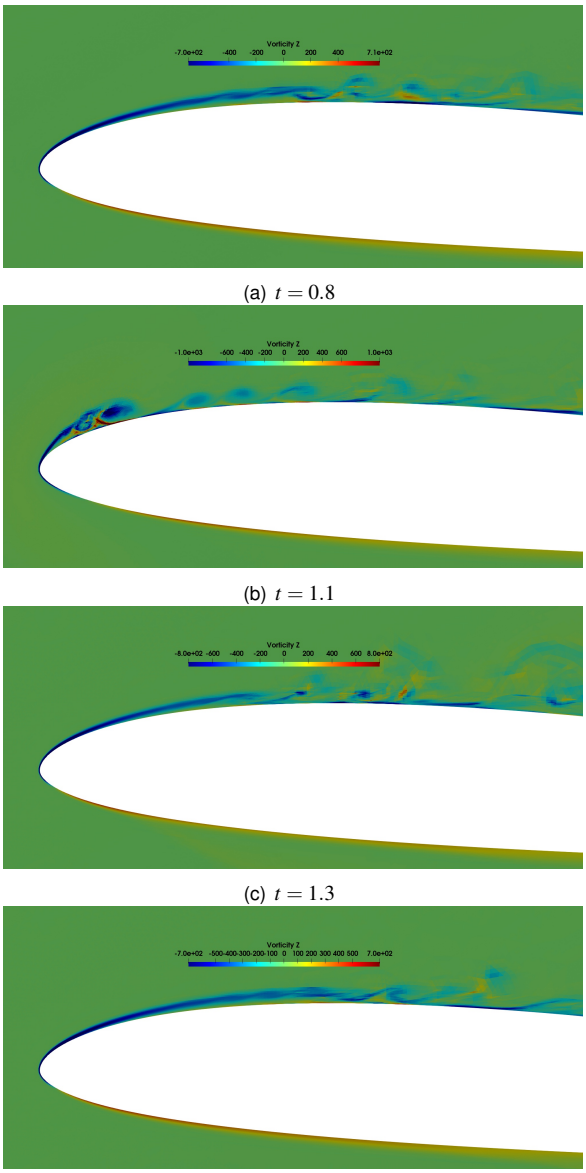

(a) $t = 0.8$

(b) $t = 1.1$

(c) $t = 1.3$

(d) $t = 1.6$

Figure 4: Spanwise component of the vorticity; from top to the bottom: before the hit of the vortex, at the instants corresponding to the maximum and the minimum lift and when the vortex is passed downstream.

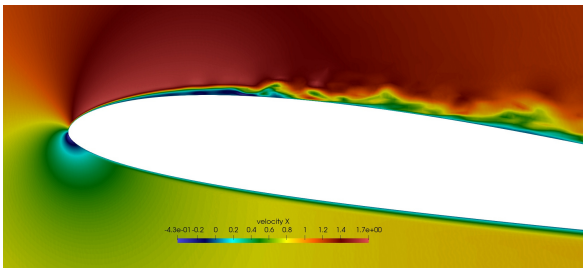

(a) $t = 0.8$

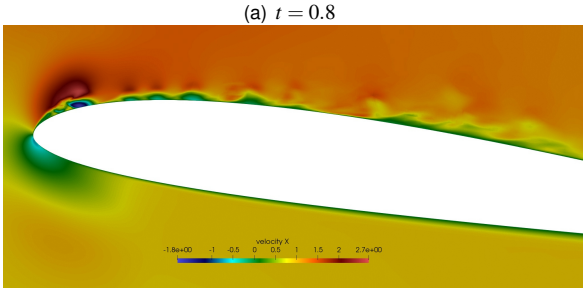

(b) $t = 1.1$

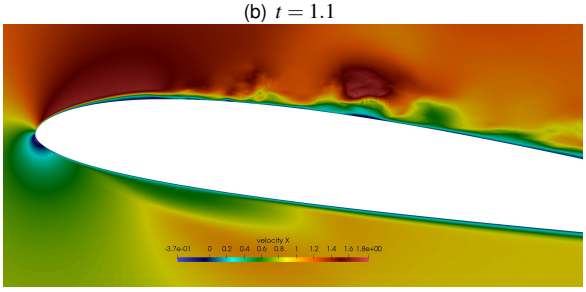

(c) $t = 1.3$

Figure 5: Streamline component of the velocity: before the hit of the vortex (left), at the instant corresponding to the maximum lift (middle) and the minimum lift (right).

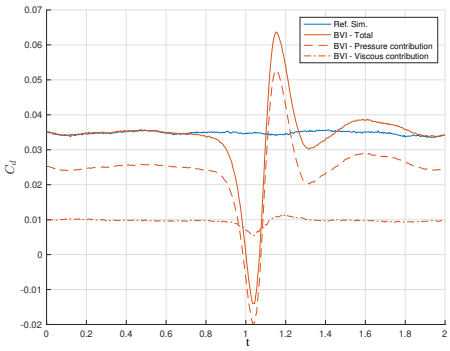

(a) Drag coefficient

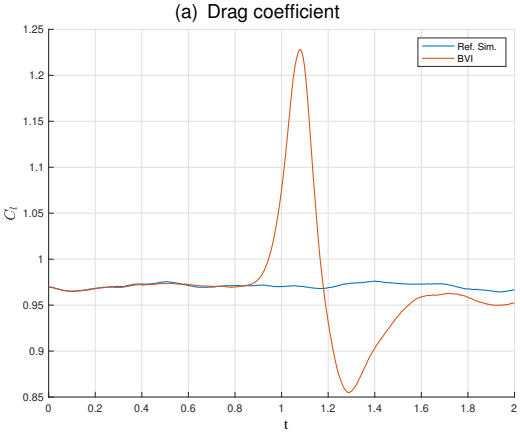

(b) Lift coefficient

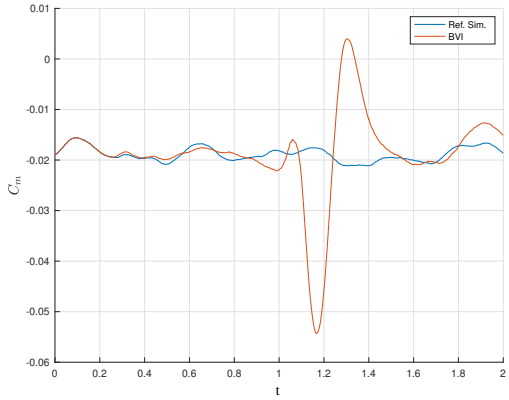

(c) Moment coefficient

Figure 6: Forces coefficients in function of time during the BVI, compared with the reference simulation without the vortex.

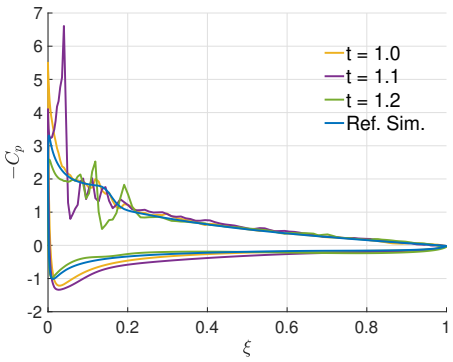

Figure 7: Pressure coefficient C_p at different times during the BVI, compared with the reference simulation without the vortex [34].

The analysis of the loads oscillations is the most interesting result from an engineering point of view and for structural analysis. The comparison between the force coefficients during BVI and the value obtained by the reference simulation without vortex [34] is showed in Figure 6. The BVI does not affect the force coefficients until $t \approx 0.8$ when the vortex is 0.4 upstream the LE. The drag is the first component of the aerodynamic force to change, decreasing to the minimum value of $C_{d,min} = -0.014$ at $t = 1.04$ when the low pressure core of the vortex acts on the LE. This is confirmed by the Figure 6(a) which demonstrates that the stronger variation in the drag is pressure-driven. Since the impinging vortex is counter-clockwise it induces an increase of incidence and as consequence the lift coefficient rises until its maximum value $C_{l,max} = 1.228$ at $t = 1.08$, corresponding to an increment of 27% the reference C_l value (see Figure 6(b)). Some different phenomena happen between $t \approx 1$ and $t \approx 1.2$ which affect the force coefficients behavior. First of all, Figure 7 shows a modified pressure distribution at $t = 1.0$ and for $0 < \xi < 0.2$, on both pressure and suction sides of the airfoil, as effect of the induced incidence, resulting in an increase of the lift coefficient. The vortex splits in two at $t \approx 1.04$ corresponds to the minimum drag. After that the low pressure core of the splitted vortices causes the minimum value of the C_p on the pressure side and the high peak on the suction side for $t = 1.1$. The secondary vortex moving on the pressure side causes pressure values higher than in the reference simulation, especially for $0 < \xi < 0.3$, as shown for $t = 1.2$ in Figure 7. Consequently the moment coefficient reaches its minimum value $C_{m,min} = -0.054$ with an increment of 190% respect to the reference value $C_m = -0.0186$ at $t = 1.17$. This minimum value of C_m is also related to a difference between the low pressure in the vortex core at $\xi \approx 0.1$ and the higher pressure for $\xi > 0.5$ caused by the acoustic wave generated by the collision of the vortex on the leading edge, as shown in Figure 8(b). This pressure difference affects also the maximum of the drag coefficient $C_{d,max} = 0.064$, for $t = 1.15$, representing an increase of 85% respect to the reference value.

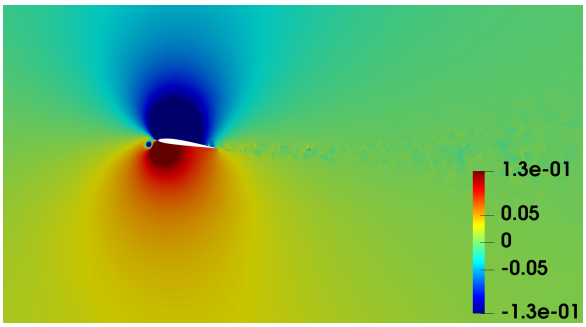

(a) $t = 0.9$

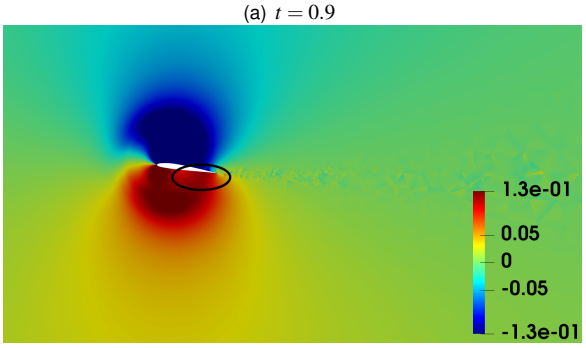

(b) $t = 1.2$

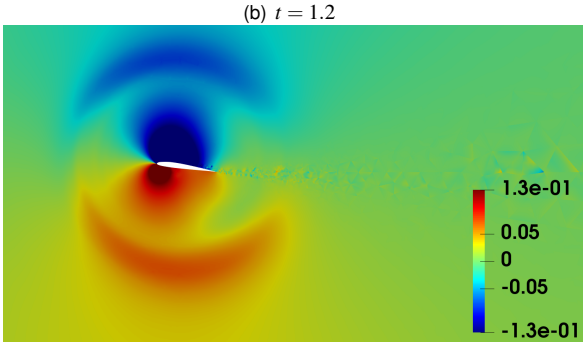

(c) $t = 1.4$

Figure 8: Visualization of the pressure perturbation $p - p_r$ in the plane $z = 0.2$ at different time t: when the vortex hit on the LE at $t = 0.9$; at $t = 1.2$ just after the minimum of C_m; at $t = 1.4$. The circle highlight the high pressure caused by the acoustic wave generated by the impact of the vortex.

The secondary vortex, moving on the suction-side, disturbs the boundary layer and generates a local separation which get the lift decreases reaching the value $C_{l,min} = 0.855$ at the time $t = 1.3$, with a defect of 18% respect to the reference value, while the moment coefficient reaches the maximum $C_{m,max} = 0.004$. Finally it is worth noting that at $t = 1.9$ the drag coefficient reaches the steady state value at $t = 1.9$, while the lift is still bit lower and, consequently, the moment coefficient is higher then the corresponding reference values. A longer simulation should be necessary to observe the end of the transient. This particular behavior is probably related to the passage of the vortex on the recirculating region on the suction side which takes time to regenerate.

4 CONCLUSIONS

The LES using the dynamic P-adaptive approach in a DG framework has been applied to the study of the parallel, viscous BVI. The results are compared with a reference simulation of the developed flow in similar conditions to show the effects of the interaction on the transitional separated region and on the aerodynamic forces. Lift, drag and moment coefficients are all strongly affected by this interaction. It is interesting to notice also the effect on the moment coefficient due to the pressure wave generated by the impact of the vortex.

5 ACKNOWLEDGMENTS

We acknowledge that the results of this research have been achieved using the computational resources made available at the CINECA supercomputing center (Italy) by the high performance computing project ISCRA-B LESDY HP10BQZQ3O.

Copyright Statement

REFERENCES

[1] R. Morvant, K.K.J. Badcock, and G.G.N. Barakos. Aerofoil-vortex interaction using the compressible vorticity confinement method. *AIAA J*, 43:63–75, 2005.

[2] Y. Tanabe, S. Saito, K. Takasaki, and H. Fujita. A parametric study of parallel blade-vortex-interaction noise. *Noise Control Eng. J.*, 57:420–433, 2009.

[3] F. Felten and T. Lund. Numerical simulation of parallel airfoil/vortex interaction using a zonal hybrid rans/les method. In *17th AIAA Computational Fluid Dynamics Conference*, 2005.

[4] M. Ilie. A fully-coupled cfd/csd computational approach for aeroelastic studies of helicopter blade-vortex interaction. *Appl. Math. Comput.*, 347:122–142, 2019.

[5] A. Abbà, A. Recanati, M. Tugnoli, and L. Bonaventura. Dynamical p–adaptivity for LES of compressible flows in a high order dg framework. *J. Comp. Phys.*, 420:109720, 2020.

[6] A. Abbà, D. Campaniello, and M. Nini. Filter size definition in anisotropic subgrid models for Large Eddy Simulation on irregular grids. *Journal of Turbulence*, 18:589–610, 2017.

[7] A.P. Broeren, P. Giguere, M.S. Selig, and J.J Guglielmo. *Summary of Low-Speed Airfoil Data. Vol. I.* SoarTech Publications, 1995.

[8] M. Tugnoli, A. Abbà, L. Bonaventura, and M. Restelli. A locally p-adaptive approach for Large Eddy Simulation of compressible flows in a DG framework. *Journal of Computational Physics*, 349:33–58, 2017.

[9] D. Rival, R. Manejev, and C. Tropea. Measurement of parallel blade–vortex interaction at low reynolds numbers. *Exp. in Fluids*.

[10] B. Cockburn and C.W. Shu. The Runge-Kutta Discontinuous Galerkin method for conservation laws, V. *Journal of Computational Physics*, 141:198–224, 1998.

[11] L. Zhang, T. Cui, and H. Liu. A set of symmetric quadrature rules on triangles and tetrahedra. *Journal of Computational Mathematics*, 27:89–96, 2009.

[12] S. S. Collis. Discontinuous Galerkin methods for turbulence simulation. In *Proceedings of the 2002 Center for Turbulence Research Summer Program*, pages 155–167, 2002.

[13] S. S. Collis and Y. Chang. The DG/VMS method for unified turbulence simulation. *AIAA paper*, 3124:24–27, 2002.

[14] F.van der Bos, J.J.W. van der Vegt, and B.J. Geurts. A multiscale formulation for compressible turbulent flows suitable for general variational discretization techniques. *Computer Methods in Applied Mechanics and Engineering*, 196:2863–2875, 2007.

[15] R.J. LeVeque. *Finite Volume Methods for Hyperbolic Problems*. Cambridge University Press, 2002.

[16] F.X. Giraldo and M. Restelli. A study of spectral element and discontinuous Galerkin methods for the Navier-Stokes equations in nonhydrostatic mesoscale atmospheric modeling: equation sets and test cases. *Journal of Computational Physics*, 227:3849–3877, 2008.

[17] R.J. Spiteri and S.J. Ruuth. A New Class of Optimal High-Order Strong-Stability-Preserving Time Discretization Methods. *SIAM Journal of Numerical Analysis*, 40:469–491, 2002.

[18] FEMilaro, a finite element toolbox. `https://bitbucket.org/mrestelli/femilaro/wiki/Home`. Available under GNU GPL v3.

[19] A. Abbà, L. Bonaventura, M.Nini, and M. Restelli. Dynamic models for Large Eddy Simulation of compressible flows with a high order DG method. *Computers & Fluids*, 122:209–222, 2015.

[20] A. Abbà, C. Cercignani, and L. Valdettaro. Analysis of Subgrid Scale Models. *Computer & Mathematics with Applications*, 46:521–535, 2003.

[21] M. Germano, U. Piomelli, P. Moin, and W. H. Cabot. A Dynamic Subgrid-Scale Eddy Viscosity Model. *Physics of Fluids*, 3:1760–1765, 1991.

[22] S. Cerutti and C. Meneveau. Intermittency and relative scaling of subgrid scale energy dissipation in isotropic turbulence. *Physics of Fluids*, 10:928–937, 1998.

[23] A. Cimarelli, A. Abbà, and M. Germano. General formalism for a reduced description and modelling of momentum and energy transfer in turbulence. *Journal of Fluid Mechanics*, 866:865–896, 2019.

[24] M. Germano. A direct relation between the filtered subgrid stress and the second order structure function. *Physics of Fluids*, 19:038102, 2007.

[25] G. Tumolo and L. Bonaventura. A semi-implicit, semi-Lagrangian, DG framework for adaptive numerical weather prediction. *Quarterly Journal of the Royal Meteorological Society*, 141:2582–2601, 2015.

[26] F. Naddei, M. de la Llave Plata, V. Couaillier, and F. Coquel. A comparison of refinement indicators for $p-$adaptive simulations of steady and unsteady flows using discontinuous Galerkin methods. *Journal of Computational Physics*, 376:508–533, 2019.

[27] F. Bassi, L. Botti, A. Colombo, A. Crivellini, A. Ghidoni, and F. Massa. On the development of an implicit high-order discontinuous galerkin method for dns and implicit les of turbulent flows. *Europ. J. Mech. - B/Fluids*, 55:367–379, 2016.

[28] P. Boom and D. Zingg. Time-accurate flow simulations using an efficient newton-krylov-schur approach with high-order temporal and spatial discretization. In *51st AIAA Aerospace Sciences Meeting*, 2013.

[29] A. Crivellini. Assessment of a sponge layer as a non-reflective boundary treatment with highly accurate gust–airfoil interaction results. *International Journal of Computational Fluid Dynamics*, 30:176–200, 2016.

[30] M. Restelli and F.X. Giraldo. A conservative Discontinuous Galerkin semi-implicit formulation for the Navier-Stokes equations in nonhydrostatic mesoscale modeling. *SIAM Journal of Scientific Computing*, 31:2231–2257, 2009.

[31] G. Lodato, P. Domingo, and L. Vervisch. Three-dimensional boundary conditions for direct and large-eddy simulation of compressible viscous flows. *Journal of Computational Physics*, 227(10):5105–5143, 2008.

[32] T. Colonius, S. Lele, and P. Moin. The free compressible vortex. *Journal of Fluid Mechanics*, 230:45–73, 1991.

[33] G. Droandi, G. Gibertini, and A. Zanotti. Perpendicular blade–vortex-interaction over an oscillating airfoil in light dynamic stall. *J. Fluids and Struct.*, 65:472–494, 2016.

[34] A.P.C. Bresciani and A. Abbà. Large eddy simulation of the transitional flow around the sd7003 airfoil and application to blade–vortex interaction. 2020.

[35] K. Wang, M.K. Gobbert, and M. Yu. A dynamically load-balanced parallel $p-$adaptive implicit high-order flux reconstruction method for under-resolved turbulence simulation. Technical Report arXiv:1910.03693v1, arXiv, 2019.

[36] M.C. Wilder and D.P. Telionis. Parallel blade–vortex interaction. *J. Fluids and Struct.*, 12:801–838, 1988.